

# Ultrasensitive refractive index sensor based on a Mach–Zehnder interferometer created in twin-core fiber

Zhengyong Li,<sup>1,†</sup> Changrui Liao,<sup>1,†</sup> Yiping Wang,<sup>1,\*</sup> Xiaopeng Dong,<sup>2</sup> Shen Liu,<sup>1</sup>  
Kaiming Yang,<sup>1</sup> Qiao Wang,<sup>1</sup> and Jiangtao Zhou<sup>1</sup>

<sup>1</sup>Key Laboratory of Optoelectronic Devices and Systems of Ministry of Education and Guangdong Province, College of Optoelectronic Engineering, Shenzhen University, Shenzhen 518060, China

<sup>2</sup>School of Information Science and Engineering, Xiamen University, Xiamen 361005, China

\*Corresponding author: ypwang@szu.edu.cn

Received May 29, 2014; revised July 18, 2014; accepted July 21, 2014;  
posted July 21, 2014 (Doc. ID 212897); published August 18, 2014

We proposed and experimentally demonstrated a twin-core fiber (TCF)-based Mach–Zehnder interferometer (MZI) to develop an ultrasensitive refractive index (RI) sensor. This fiber MZI was constructed by splicing a short section of TCF between two sections of single mode fibers. A microchannel was drilled through one core of the TCF by means of femtosecond laser micromachining to create one arm of the proposed interferometer, and the other core worked as the second arm. Such a fiber interferometer exhibits an ultrahigh RI sensitivity of  $-10981$  nm/RIU and a low temperature cross-sensitivity of  $3.96 \times 10^{-6}$  RIU/°C. Moreover, the ultra-compact device size and all-fiber configuration make it very suitable for highly sensitive RI sensing at precise location. © 2014 Optical Society of America

OCIS codes: (060.2370) Fiber optics sensors; (140.3390) Laser materials processing; (140.3948) Microcavity devices.  
<http://dx.doi.org/10.1364/OL.39.004982>

Recently, refractive index (RI) sensors based on optical fiber have been extensively investigated and used in various areas of biomedicine, automotive industries, and environmental monitoring. Among them, fiber in-line Mach–Zehnder interferometers (MZIs) are of great interest because of their compact size, high RI sensitivity, immunity to electromagnetic interference, and easy signal detection [1]. So far, many fiber MZI configurations have been realized such as employing long period fiber gratings [2–5], fiber tapers [6,7], offset fusion splicing [8], microfiber-based structures [9,10] and microcavity fabricated by femtosecond (fs) laser micromachining [11,12]. The microcavity-based MZI sensors exhibit much higher RI sensitivities than the other MZI configurations because the optical path difference (OPD) is achieved through light propagation across the fluid-filled cavity, which gives a large effective RI difference.

Fs laser micromachining is an efficient tool for material processing, especially in the fabrication of optical fiber devices, because of its high fabrication efficiency and accurate material processing capability. Several fiber interferometers based on fs-laser induced microcavity have been achieved and used for RI and temperature sensing. Liao *et al.* have reported a highly sensitive RI fiber sensor ( $\sim 9148$  nm/RIU), which is based on an in-fiber microcavity fabricated by fs laser ablation [13]. However, two arms of the interferometer are not independent of each other so that the measurement accuracy would deteriorate a lot because of the cross talk between the two arms. To overcome this issue, we employ twin-core fiber (TCF) in this work. TCFs are suitable to construct compact fiber in-line interferometers because there are two separate cores being integrated in the same fiber. Several fiber interferometric sensors, which are based on TCFs, have been developed and used for measurement of the RI [14] and curvature [15].

In this Letter we demonstrate an ultra-compact TCF-based MZI, which is fabricated by the means of fs laser micromachining. The fiber interferometer is constructed by splicing a short section of TCF between two SMFs, and the separate cores of the TCF perform as the two interference arms. One arm contains a microchannel, which is created by removing part of one core of the TCF, and the second arm is the other complete core. This TCF-based MZI exhibits an ultrahigh RI sensitivity of  $-10981$  nm/RIU within the RI range between 1.30 and 1.34 and a low cross-sensitivity to a temperature of  $3.96 \times 10^{-6}$  RIU/°C. Moreover, the ultra-compact size of the fiber interferometer is able to ensure a precise sensing location.

The schematic diagram of the proposed TCF-based MZI is illustrated in Fig. 1. The light propagating in SMF<sub>1</sub> is divided into two beams in the TCF, which are denoted as  $I_{in1}$  and  $I_{in2}$ , respectively.  $I_{in1}$  remains propagating in core<sub>1</sub> of the TCF while  $I_{in2}$  travels through the microchannel embedded in core<sub>2</sub>. When the two output beams, i.e.,  $I_{out1}$  and  $I_{out2}$  corresponding to  $I_{in1}$  and  $I_{in2}$ , recombined in SMF<sub>2</sub>, the interference will take place because of the phase difference between two output beams. The output intensity of TCF-based MZI can be expressed as

$$I = I_{out1} + I_{out2} + 2\sqrt{I_{out1}I_{out2}} \cos\left(\frac{2\pi L\Delta n}{\lambda} + \varphi_0\right), \quad (1)$$

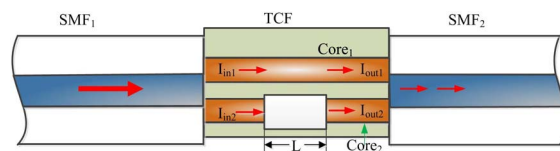


Fig. 1. Schematic diagram of the TCF-based MZI.

where  $\lambda$  is the light wavelength,  $L$  is the length of the microchannel,  $\Delta n = n_{\text{core}} - n_{\text{channel}}$  is the effective RI difference between two interference arms, where  $n_{\text{core}}$  and  $n_{\text{channel}}$  are the effective RI of the core mode and the channel mode, and  $\varphi_0$  is the initial phase of the interference. According to Eq. (1), the interference signal reaches the minimum value when the following condition is satisfied:

$$\frac{2\pi L \Delta n}{\lambda_m} + \varphi_0 = (2m + 1)\pi, \quad (2)$$

where  $m$  is an integer, and  $\lambda_m$  is the wavelength of the  $m$ th order interference dip. The free spectral range (FSR) of such fiber interferometer can be expressed as

$$\text{FSR} = \frac{\lambda^2}{\Delta n L}. \quad (3)$$

The device fabrication involves two steps. First, one end of the TCF was spliced with an SMF (Corning, SMF-28) with a core/cladding diameter of 8/125  $\mu\text{m}$  by using a commercial fusion splicer (Fujikura FSM-60s). The cross-sectional morphology of the TCF supplied by Xiamen University is shown in Fig. 2(a), where the cladding diameter is 125  $\mu\text{m}$  and the major axis and minor axis of the two elliptical cores are measured to be  $\sim 10.9$  and  $\sim 6.5$   $\mu\text{m}$ , respectively. During the splicing, the red laser beam was launched into the SMF<sub>1</sub> and the light intensity of two TCF cores was compared by using an optical microscope. The offset distance between SMF<sub>1</sub> and TCF was carefully adjusted to make sure the light intensity in the two cores becomes roughly equal. Figures 2(b) and 2(c) show the unequal and equal splitting ratios when different offsets are employed. In the experiment the TCF with a length of  $\sim 200$   $\mu\text{m}$  was used and the other end of the TCF was spliced with another SMF<sub>2</sub> with an optimized offset value to obtain the maximum intensity output.

Second, a microchannel was drilled in the TCF by means of fs laser micromachining. The schematic diagram of fs laser micromachining system is shown in

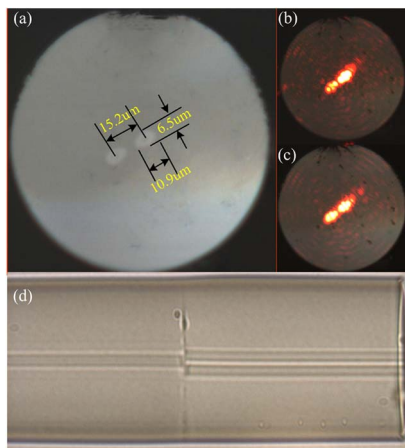


Fig. 2. (a) Optical microscope image of the cross-sectional morphology of the TCF; (b) unequal intensity distribution on the end face of TCF; (c) equal intensity distribution on the end face of TCF; (d) splicing point between SMF and TCF.

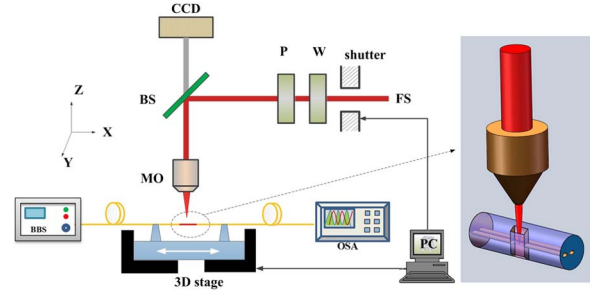


Fig. 3. Schematic diagram of the fs laser micromachining system, which is employed to fabricate in-fiber structure.

Fig. 3. The fs laser (Spectra-Physics, Solstice) with the wavelength of 800 nm, the pulse duration of 120 fs, and the repetition rate of 1 kHz was employed. A laser beam was focused onto the fiber by an objective lens with an NA value of 0.25. The laser power was adjustable in the range between 0 and 4 mJ by rotating a half-wave plate followed by a polarizer, and the average on-target laser power was maintained at  $\sim 20$  mW. A broadband light source (BBS) and an optical spectrum analyzer (OSA) were connected to the fiber to measure its transmission spectrum in real time.

The fiber was fixed on a PC-controlled three-axis (XYZ) translation stage with a resolution of 10 nm, in parallel with the Y axis. The laser beam was initially focused into the center of the core<sub>2</sub> of TCF and then shifted by 15  $\mu\text{m}$  away from the Y axis. The microchannel was directly drilled by fs laser ablation, scanning in parallel with Y axis at a speed of 5  $\mu\text{m}/\text{s}$  with the scanning distance of 40  $\mu\text{m}$  along the fiber axis and then returned to the starting point, which is definite to be one scanning cycle. After each scanning cycle, the focal point of the laser beam was moved toward the core along the Y axis with a step of 3  $\mu\text{m}$  before the next cycle started. When the interference spectrum emerged, the step was reduced to 1  $\mu\text{m}$  until the expected transmission spectrum was obtained. Finally, the microchannel was cleaned by using alcohol after laser fabrication. The optical microscope images of the microchannel in two perpendicular directions were shown in Fig. 4. To learn the real size of the microchannel at the fiber core, the sample was first immersed into the oil with a similar RI to silica in order to improve the image quality and then the microscope focus was moved from the fiber top surface to the core. The rough size of the microchannel at the core can be observed in Fig. 4(a). To learn the accurate size of the microchannel, we need to cut off the microchannel to observe the cross-sectional morphology as shown in

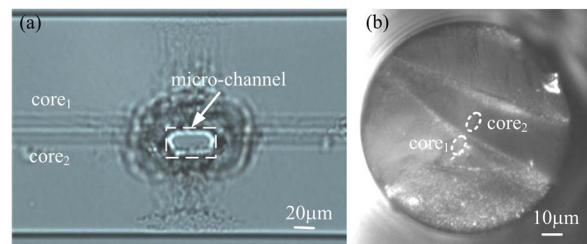


Fig. 4. Optical microscope images of the microchannel from (a) the top view and (b) the side view.

Fig. 4(b). The relatively large surface roughness implies that the employed laser power was somewhat high. Better surface quality may be achieved by optimizing the processing parameters, including laser power and scanning speed [12].

The transmission spectrum in the air of the MZI with a microchannel of 43  $\mu\text{m}$  in length is denoted by the black line in Fig. 5(b), where an insertion loss of  $\sim 10$  dB and a fringe visibility of  $\sim 17$  dB are achieved. There might be three factors causing the large insertion loss: (1) the laser induced rough surface; (2) the loss from the unguided mode propagating through the microchannel; and (3) the loss from fusion splicing. By optimizing the parameters in fusion splicing and laser micromachining, the insertion loss may be decreased to a large degree. Moreover, the insertion loss of this device will also decrease when it is immersed into the liquid because the reduced RI difference at the surface of the microchannel suppresses the scattering loss.

Polarization dependent loss (PDL) of the above sample in C-band was measured by an All Optical Parameter Analyzer (from Agilent) and the result is displayed in Fig. 5(b), where the maximum PDL is  $\sim 1$  dB. Thus, we can say this type of fiber interferometer shows a low polarization dependency.

Equation (3) indicates that there is an inversely proportional relationship between the FSR and the length of the microchannel so that the FSR value could be optimized by adjusting the length of the microchannel at a given operation wavelength. To experimentally study the relationship between the FSR and the microchannel

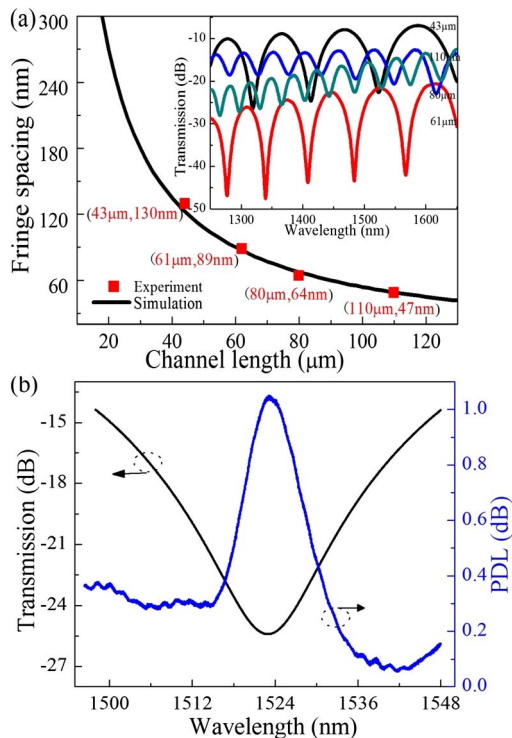


Fig. 5. (a) Fringe spacing as a function of the microchannel length at 1550 nm. Inset: transmission spectra of the TCF-based MZIs with microchannel lengths of 43, 61, 80, and 110  $\mu\text{m}$ ; (b) transmission spectrum and PDL of the TCF-based MZI with the microchannel length of 43  $\mu\text{m}$  in the air.

length, four TCF-based MZIs with different microchannel lengths, i.e., 43, 61, 80, and 110  $\mu\text{m}$ , have been fabricated and measured in air ( $n_{\text{channel}} = 1.00$ ), the corresponding transmission spectra are displayed in Fig. 5(b). Assuming  $n_{\text{core}} = 1.445$  (at 1550 nm), the relationship between the FSR and the microchannel length can be calculated as the black line displayed in Fig. 5(a) and the measured FSR of the four samples at 1550 nm is denoted by the red squares. There is a small deviation between the experimental data and the calculated one that might be explained by the measurement error of the microchannel length in experiment.

The RI response of the TCF-based MZI has been investigated by immersing it into a series of RI liquids (Cargille Labs, <http://www.cargille.com>) in a RI range from 1.300 to 1.340 with an interval of 0.005 at room temperature. The transmission spectrum was recorded by using an OSA with a resolution of 0.02 nm. Each time the sensor was taken out from the tested liquid, it should be carefully cleaned by alcohol to completely remove the residual liquid. When the spectrum returns to the initial state in air, a new round test can be carried out.

Figure 6(a) shows the transmission spectra of the TCF-based MZI with the microchannel length of 43  $\mu\text{m}$  in different RI liquids and it can be found that the fringe dip experienced a significant blue shift with an increase of the liquid RI. The wavelength of the fringe dip and insertion loss varying with the liquid RI is illustrated in Fig. 6(b), where the insertion loss hardly changed with RI but a good linear wavelength response with an ultrahigh sensitivity of  $-10981$  nm/RIU was obtained. Different from other fiber in-line MZIs reported previously, the TCF-based MZI results from the interference between the guided mode in  $\text{core}_1$  and the unguided mode traveling through the microchannel in  $\text{core}_2$ . The effective RI difference between two interferometer

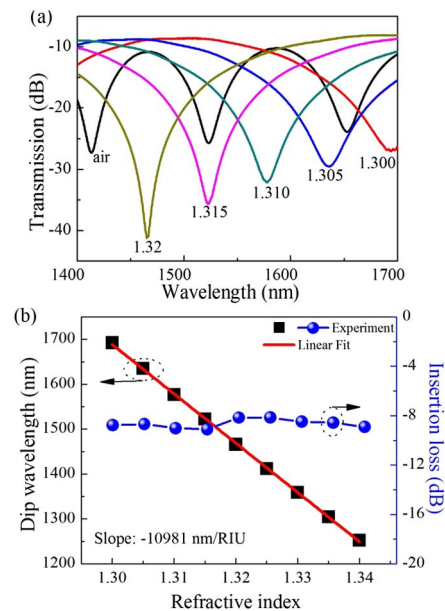


Fig. 6. (a) Transmission spectral evolution within the wavelength range from 1400 to 1700 nm when the surrounding RI changes from 1.0 (in air) to 1.32; (b) Dip wavelength and insertion loss vary with RI.

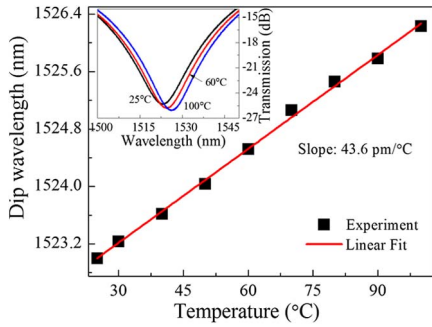


Fig. 7. Wavelength shift of the fringe dip with the temperature varying from 25°C to 100°C. Inset: the evolution of the transmission spectrum with temperature variation.

arms is large ( $\Delta n > 0.1$ ), which guarantees an ultrahigh RI sensitivity.

Assuming that the microchannel length is a constant, the RI sensitivity can be derived from Eq. (2) as  $d\lambda/d(\Delta n) = \lambda/\Delta n$ . This illustrates that the RI response of the TCF-based MZI only depends on the operation wavelength and the RI difference between the core and the medium in microchannel but has nothing to do with the microcavity length. The RI sensitivity is calculated to be  $\sim 10690$  nm/RIU at 1550 nm for  $\Delta n = 1.445 - 1.30 = 0.145$ , which is very close to the experimental result.

Some similar schemes include the MZI fabricated by side-ablating a U-shape microcavity in an SMF [16] and the one fabricated by drilling a hole through an SMF but an RI cross-talk ( $\delta$ ) cannot be avoided in RI test. The RI difference between two interference arms has a modified expression as  $\Delta n' = n_{\text{core}} + \delta - n_{\text{cavity}}$ , which will reduce its RI sensitivity. Differently, the TCF-based MZI proposed here employs two independent arms to overcome the cross-talk to further increase the RI sensitivity. Besides, the large RI difference of the two arms makes the TCF-based MZI more compact.

It is known that the best visibility can be obtained when the light intensity of the two interference beams is equal. For the TCF-based MZI, the first splicing point between SMF<sub>1</sub> and TCF equally splits the input light ( $I_{\text{in}1} \approx I_{\text{in}2}$ ). The employed TCF is very short in length so that the light coupling between the two cores could be neglected, that is to say, the input light in the two cores of the TCF is able to propagate independently. In the core<sub>2</sub> the microchannel has introduced a large insertion loss for the output beam ( $I_{\text{out}2}$ ) and hence a poor visibility is obtained. However, when the microchannel is filled with liquid, the decreased RI difference reduces both the propagation loss of the unguided mode and the surface scattering loss. Thus,  $I_{\text{out}2}$  is increased to approach  $I_{\text{out}1}$  to improve the fringe visibility.

The influence of temperature on the fiber sensor has been investigated by placing it into an electrical oven and gradually increasing the temperature from room temperature to 100°C. The inset of Fig. 7 shows the transmission spectra of the fiber sensor at 25°C, 60°C, and 100°C and a red shift is clearly observed when the temperature is increased. A wavelength shift of the interference dip at  $\sim 1525$  nm with temperature variation is displayed in Fig. 7, where a linear relation is found and

the temperature sensitivity obtained is at  $\sim 43.6$  pm/°C. When the medium in microchannel is air,  $n_{\text{channel}}$  is a constant ( $n_{\text{channel}} = 1$ ) for different temperatures. The temperature sensitivity of the TCF-based MZI is mainly determined by the thermo-optical coefficient of the core. When no temperature compensation is employed in practical measurement, the error resulting from temperature cross-sensitivity is  $3.96 \times 10^{-6}$  RIU/°C.

In conclusion, we have experimentally demonstrated an ultra-compact TCF-based MZI for RI measurement with extremely high sensitivity and precise sensing location. The two cores of the TCF performed as two interference arms and a microchannel was drilled through one core by means of an fs laser micromachining and the microchannel worked as the sensing region. Such a TCF-based MZI exhibits an ultrahigh RI sensitivity of  $-10981$  nm/RIU in the RI range from 1.30 to 1.34 and a low temperature cross-sensitivity of  $3.96 \times 10^{-6}$  RIU/°C. It is suitable to the applications in the fields of chemical/biomedical sensing and environmental monitoring.

This work was supported by the National Natural Science Foundation of China (grants no. 11174064, 61308027, and 61377090), Natural Science Foundation of SZU (no. 801-00036401), Science & Technology Innovation Commission of Shenzhen (grants no. KQCX20120815161444632 and JCYJ20130329140017262), and Distinguished Professors' Funding from Shenzhen University and Guangdong Province Pearl River Scholars.

<sup>†</sup>These authors contributed equally to this work.

## References

- Z. Li, Y. Wang, C. Liao, S. Liu, J. Zhou, X. Zhong, Y. Liu, K. Yang, Q. Wang, and G. Yin, *Sens. Actuators B* **199**, 31 (2014).
- S. W. James, I. Ishaq, G. J. Ashwell, and R. P. Tatam, *Opt. Lett.* **30**, 2197 (2005).
- Y. P. Wang, Y. J. Rao, Z. L. Ran, T. Zhu, and X. K. Zeng, *Opt. Lasers Eng.* **41**, 233 (2004).
- Y. Wang, *J. Appl. Phys.* **108**, 081101 (2010).
- Y. Wang, J. Chen, and Y. Rao, *J. Opt. Soc. Am. B* **22**, 1167 (2005).
- B. Li, L. Jiang, S. Wang, J. Yang, M. Wang, and Q. Chen, *Opt. Laser Technol.* **44**, 640 (2012).
- J. Yang, L. Jiang, S. Wang, B. Li, M. Wang, H. Xiao, Y. Lu, and H. Tsai, *Appl. Opt.* **50**, 5503 (2011).
- J. Zhou, C. Liao, Y. Wang, G. Yin, X. Zhong, K. Yang, B. Sun, G. Wang, and Z. Li, *Opt. Express* **22**, 1680 (2014).
- T. Y. Hu and D. N. Wang, *Opt. Lett.* **38**, 3036 (2013).
- C. R. Liao, D. N. Wang, and Y. Wang, *Opt. Lett.* **38**, 757 (2013).
- Y. Jung, S. Lee, B. H. Lee, and K. Oh, *Opt. Lett.* **33**, 2934 (2008).
- Y. Wang, M. Yang, D. N. Wang, S. Liu, and P. Lu, *J. Opt. Soc. Am. B* **27**, 370 (2010).
- C. R. Liao, W. Ying, D. N. Wang, and M. W. Yang, *IEEE Photon. Technol. Lett.* **22**, 1686 (2010).
- G. Yin, S. Lou, and H. Zou, *Opt. Laser Technol.* **45**, 294 (2013).
- G. Yin, S. Lou, W. Lu, and X. Wang, *Appl. Phys. B* **115**, 6 (2014).
- L. Zhao, L. Jiang, S. Wang, H. Xiao, Y. Lu, and H.-L. Tsai, *Sensors* **11**, 54 (2011).